Article

Characterization of a Chromium-Bearing Carbon Steel Electric Arc Furnace Slag after Magnetic Separation to Determine the Potential for Iron and Chromium Recovery

Kathy Bru [1,*], Alain Seron [1], Agnieszka Morillon [2], David Algermissen [2], Catherine Lerouge [1] and Nourredine Menad [1,*]

[1]   BRGM, F-45060 Orléans, France; a.seron@brgm.fr (A.S.); c.lerouge@brgm.fr (C.L.)
[2]   FEhS, 47229 Duisburg, Germany; a.morillon@fehs.de (A.M.); d.algermissen@fehs.de (D.A.)
[*]   Correspondence: k.bru@brgm.fr (K.B.); n.menad@brgm.fr (N.M.); Tel.: +33-2386-44761 (K.B.)

Abstract: This study investigates the potential to recover iron and chromium from a chromium-bearing carbon steel Electric Arc Furnace (EAF) slag. This slag contains indeed about 30 wt.% Fe and 2.5 wt.% Cr. However, the minerals are intergrown at small scale (<100 μm) and iron and chromium are mostly contained in spinel phases which makes the separation challenging. Several methods including Mössbauer spectroscopy, X-ray Diffraction, Scanning Electron Microscopy (SEM) and electron microprobe analysis were used in order to fully characterize the products obtained after a low-intensity magnetic separation of this carbon steel EAF slag, with the objective to define a pre-treatment process allowing the recovery of iron-rich particles and of a chromium-upgraded fraction. The results show that even if the magnetic separation seems to be not efficient in a first approach for producing an iron-rich/chromium-poor fraction, this fraction can be obtained by adding an attrition step which means that some separation mechanisms still occurred during the magnetic separation. However, it was not possible to produce a chromium-rich fraction. The main bottleneck for reaching a good separation is most probably the very fine liberation size of the iron and chromium bearing minerals.

Keywords: Electric Arc Furnace slag; magnetic separation; attrition; multi-analytical characterization

1. Introduction

Ferrous slags are one of the main by-products of the steel industry. Depending on the iron and steel production process, different types of slags are produced. In particular, Blast Furnace Slag (BFS) is made during the melting and reduction in iron ore in a blast furnace and steel slag is generated either by converting pig iron to steel in Basic Oxygen Furnace (BOF) or from the melting of scrap to produce steel in Electric Arc Furnace (EAF) either for carbon (C EAF) or for stainless/high-alloy steel production (S EAF). In Europe, according to EUROSLAG data (European Association representing metallurgical slag producers and processors), 34.9 million tons of slag were produced in 2018, of which 19.2 million tons are BFS and 15.7 million tons are steel slag [1]. Details regarding the production of steel slags in Europe in 2018 are given in Table 1.

Table 1. Steel slag production in Europe, year 2018 [1].

Type of Steel Slags	Production (Million Tons)	%
BOF slag	8.3	52.7
EAF slag (carbon steel)	4.1	26.3
EAF slag (high-alloy steel)	1.3	8.5
Secondary steel slag	2.0	12.5

Most of the ferrous slags are valorized. In particular regarding the steel slags, the main application with almost 70% of used slag is the production of aggregates for road construction (respectively, 51% of the total steel slag production in 2018). Other applications include cement or concrete addition, fertilizer, hydraulic engineering and internal use for metallurgical purposes. About 12.7% were sent to a final deposit in 2018, mostly due to their fine grain size, volume expansion and environmental issues related to heavy metal leaching [1]. Particularly for cement and concrete application, the slags must be very volume stable [2]. The usage as fertilizer is often limited [3] due to too high heavy metal contents or the reuse of slag is prevented by defining the material in general as waste [4].

The main chemical components of EAF slag are iron oxides (FeO, Fe_2O_3), lime (CaO), silica (SiO_2), magnesia (MgO) and alumina (Al_2O_3). Minor components include chromium, manganese, phosphorus oxides as well as small amounts of free lime and critical metals [5–7]. The composition of the EAF slags varies from steel plant to steel plant, and sometimes even within a steel plant. The most important aspects that influence the resulting physical and chemical composition are the raw materials (such as origin and types of scraps, additions), the steel production process, the types of products which are produced (i.e., carbon steels, alloy steels, stainless steels) and the slag cooling process [6,8,9].

The presence of some elements such as chromium (Cr), which comes from the ferrous scraps, can impede the reuse of steel slags. Chromium is commonly found in two oxidation states, namely Cr(III) and Cr(VI), and while the trivalent form, Cr(III), is a non-toxic and non-hazardous element, Cr(VI) is highly toxic and is classified as a hazardous material. The speciation not only affects toxicology, but also the mobility and availability of Cr, with Cr(VI) compounds being much more mobile and bioavailable than the stable and almost insoluble Cr(III) compounds [10]. In most regulations, a leaching test on the material is prescribed, with a limitation of toxic substances contained in the eluate [6]. On the other side, chromium is a valuable metal, and therefore, chromium-containing slags can be considered as a secondary source of metal [11]. Investigating the possibility to recover the chromium contained in steel slags is then interesting from an environmental an economic point of view. Currently, the treatment process of steel slags includes several steps of crushing and screening combined with magnetic separation steps in order to recover the metallic particles which are recycled into the steelmaking process. Chromium is then not recovered. Project CHROMIC (effiCient mineral processing and Hydrometallurgical RecOvery of by-product Metals from low-grade metal contaIning seCondary raw materials), which was funded by the European Union's Horizon 2020 Research and Innovation program, investigated the potential for recovering Cr from slags by a combination of physical pre-treatment and hydrometallurgical processes.

One of the samples studied within the project CHROMIC is a carbon steel EAF slag. This slag is characterized by the intertwining at small scale (<100 μm) of the minerals, the main ones being Ca(Al) silicates (larnite, gehlenite) and Fe oxides, including Fe-based spinel phases (magnetite, Fe-Mg spinel) [12]. Horckmans et al. [12] also showed that the chromium is unevenly distributed within the spinels. Even if the iron content was measured to be about 30%, the small size of the Fe-rich particles makes their recovery challenging with magnetic separation techniques.

In this study, several methods have been used to characterize the products obtained after a low-intensity magnetic separation of a carbon steel EAF slag. The objective is to identify the potential of this technique not only for the recovery of iron particles which could then be re-used for steelmaking but also for the production of a Cr-upgraded fraction which could be used as a basis for chromium recovery.

2. Materials and Methods

2.1. Materials

The carbon steel EAF slag used in this study was provided by a European slag processor. Details about the characterization of this carbon steel EAF slag are given by Horckmans et al. [12]. Its main components, determined by X-ray Fluorescence (XRF), are Fe

(30.0 wt.%), Ca (14.6 wt.%), Si (4.6 wt.%), Al (4.3 wt.%), Mn (4.3 wt.%), Mg (2.1 wt.%) and Cr (2.5 wt.%). Regarding its mineralogical composition, it contains 26.7 wt.% of spinels with various compositions, 32.6% of Ca-silicates such as larnite (17.8 wt.%) and gehlenite (14.8 wt.%), 14.8 wt.% of wüstite and 4.0 wt.% of hematite. Most of the spinels are Mg-Fe-containing spinels (magnesioferrite, $MgFe_2O_4$, 17 wt.%), magnetite (Fe_3O_4, 5 wt.%) and magnesiochromite ($MgCr_2O_4$, 3 wt.%). This slag is characterized by the intergrowth of minerals at small scale (<100 µm), with the Cr-rich spinels being 10–100 µm in size. Larger Fe-oxide particles were also identified around complex mixtures of Ca-silicates, spinels and Cr-rich spinels.

2.2. Experimental Set-Up

Magnetic separation was performed at low intensity (0.1 T) on dried samples. The carbon steel EAF slag was previously crushed using jaw crushers down to 2 mm with recovery of metallic particles at coarser sizes, sieved at 0.25 mm to remove the fines and screened at 1 mm in order to have narrow fractions for the separation step (i.e., +0.25–1 mm and +1–2 mm). The mass balance of this crushing step is given in Table 2. The Low Intensity Magnetic Separation (LIMS) was then performed on the two size fractions (+0.25–1 mm and +1–2 mm). The non-magnetic fractions were processed again with the same magnetic separator in order to increase the recovery of the magnetic particles. All the magnetic fractions were then gathered together as well as all the non-magnetic fractions.

Table 2. Mass balance of the crushing down to 2 mm (wt.%).

+0–0.25 mm	+0.25–1 mm	+1–2 mm	+ 2 mm (Metallic Particles)
10.2	27.2	57.8	4.8

Attrition was performed on the magnetic and non-magnetic fractions in a batch dry rod mill working at 43 rpm. Attrition was carried out on a sample of about 4.3 kg with a rod charge fixed at 31 kg. For the magnetic fraction, 3 durations of the attrition were tested: 20 min, 40 min and 60 min. For the non-magnetic fraction, attrition was only performed during 40 min. After attrition, the material was manually sieved at 4 sizes (2 mm, 1 mm, 0.5 mm, 0.25 mm).

2.3. Characterization Method

The Fe and the Cr content of the samples was measured by X-ray Fluorescence (XRF) (Niton handheld analyzer, Fondis), calibrated against in-house standards, on samples finely ground. The detailed composition of samples was determined according to DIN EN 13656. For the total chemical composition, 100 mg of sample finely ground (<63 µm) was digested with HNO_3, HF and H_2O_2 in a microwave for 2×20 min, followed by 20 min microwave digestion with H_3BO_3. For the Fe metal, a softer extraction method was chosen by digesting 500 mg of sample with bromine-methanol extraction in a microwave for 1 h in order to digest only metallic fraction. The eluates were analysed with ICP-OES ("Varian Vista MPX" and "Spectro Ciros"), with analytical error of 3%.

Mineral composition was determined by X-ray Diffraction (XRD). These analyses were performed on representative splits of each sample after fine grinding (<63 µm). XRD was performed over the 10–80° 2θ using Cu-Kα radiation, at 40 keV and 40 mA; 2θ with a step of 0.02° and counting time of 0.5 s per step by using a Bruker D8 Advance θ/2θ diffractometer equipped with a Lynxeye energy-dispersive one-dimensional detector (Bruker, Billerica, MA, USA). Data were then exploited using DIFFRAC Suite software from Siemens. The quantitative analysis was carried out according to the Rietveld simulation from the XRD diffractogram. Similar amounts of zinc oxide powder were added to all samples to be able to compare intensity of all spectra with ZnO as reference solid to normalize intensity of spectra.

The studies of morphological aspects and element distribution were performed by coupling Scanning Electron Microscopy and Energy Dispersive X-ray Spectroscopy (SEM-EDX) analysis using a TESCAN Mira3XMU (TESCAN, Brno, Czech Republic) equipment operating at 15–25 kV with an EDAX ApolloXPP EDS detector (EDAX, Mahwah, NJ, USA). For these observations and analysis, samples were embedded in a low-viscosity epoxy resin, polished and then coated with a conductive carbon layer to inhibit charging effect and to improve the secondary electron signal used for morphology observations. These analyses were performed in order to understand the interaction between mineralogical phases and to determine the nature of the chromium bearing minerals.

In order to define the structural formula of the major phases, electron microprobe analysis was performed on the polished sections of the samples using a Camebax SX five electron microprobe (Cameca, Geneville, France) with an acceleration voltage of 20 kV and a current beam of 50 nA. The program included analysis of Mg, Si, Al, P, Ca, V, Cr, Fe, Mn, Ni, Zn, and Mo. P Kα, Ca Kα, Cr Kα were monitored on PET crystal, Fe Kα and Mn Kα on LIF crystal, Mg Kα, Si Kα, and Al Kα on TAP crystal, V Kα and Mo Lα on LPET large crystal, and Ni Kα and Zn Kα on LLIF crystal. The system was calibrated with a variety of oxide and mineral standards: Al_2O_3 for Al, apatite for P, ZnO for Zn, wollastonite for Si and Ca, YVO_4 for V, Cr_2O_3 for Cr, Fe_2O_3 for Fe, MnTi for Mn, Ni metal for Ni and Mo metal for Mo. Matrix corrections were made with a ZAF computing program.

Finally, Mössbauer spectroscopy was used to study the chemical state of the iron atoms (speciation of iron). ^{57}Fe Mössbauer spectra were collected using a conventional spectrometer in transmission geometry coupled with a cold head cryostat from Advances Research Systems (USA), equipped with vibration isolation stand, developed in LCPME (Laboratoire de Chimie Physique et Microbiologie pour les Matériaux et l'Environnement) laboratory. The 50 mCi ^{57}Co in Rh matrix radioactive source was mounted in a constant acceleration velocity transducer. Measurements were taken at the wide range of velocity ± 11 mm·s^{-1}. The hyperfine interaction parameters were determined by fitting the experimental spectra by a least-squares method using the Recoil software [13]. The center shifts were reported with respect to that of 25 μm-thick α-Fe foil at room temperature.

3. Results and Discussion

3.1. Magnetic Separation and Attrition Steps

Magnetic separations were performed on the size fraction +0.25–1 mm and +1–2 mm. Results show that the magnetic and the non-magnetic fractions have a similar Fe and Cr content, whatever the size fraction considered (Table 3). Magnetic separation seems then not to be efficient for recovering a Fe-rich or Cr-rich stream. This may be due to the very fine liberation size of the minerals and to the fact that most of the iron is in wüstite and spinels phases, the latter containing also most of the chromium, these phases being not easily recoverable with a traditional magnetic separation. However, when magnetic separation was combined with an attrition step of 40 min duration, it can be seen that attrition of the magnetic fraction led to the production of particles +1–2 mm with a Fe content of 85.9% and a Cr content of 0.6%, while this size fraction was totally ground after the attrition of the non-magnetic fraction (Table 4). The two fractions obtained after magnetic separation are then different even if they have a similar Fe and Cr content.

In order to better understand the effect of the attrition on the magnetic fraction, several durations of the attrition were investigated. Results are given in Table 5 and show that an increase in the attrition duration led to an increase in the Fe content and a decrease in the Cr content in the fraction +1–2 mm. Only minor changes were observed in the Fe and Cr content of the other size fractions with the increase in the attrition duration, except for the size fraction +0.5–1 mm in which a marked increase in the Fe content was observed after an attrition step of 60 min. These results show that these concentration steps do not allow a Cr-rich fraction to be produced. This is most probably due to the very fine liberation size of the chromium bearing minerals.

Table 3. Mass balance of the magnetic separation.

		Mass wt.%	%	Fe %Distrib.	%	Cr %Distrib.
Fraction +0.25–1 mm	Magnetic fraction	43.6	32.7	44.4	2.5	42.3
	Non-magnetic fraction	56.4	31.7	55.6	2.6	57.7
	Reconstituted	100.0	32.1	100.0	2.5	100.0
Fraction +1–2 mm	Magnetic fraction	38.9	32.7	39.5	2.5	37.8
	Non-magnetic fraction	61.1	31.8	60.5	2.6	62.2
	Reconstituted	100.0	32.2	100.0	2.6	100.0

Table 4. Mass balance of the attrition step performed during 40 min on the magnetic and non-magnetic fractions.

			Magnetic Fraction								
		Before Attrition *						After Attrition			
	wt.%	%	%Fe %Distrib.	%	%Cr s%Distrib.	wt.%	%	%Fe %Distrib.	%	%Cr %Distrib.
1–2 mm	54.5	32.0	54.7	2.5	55.4	3.1	85.9	7.6	0.6	0.7
0.5–1 mm	29.7	31.6	29.3	2.5	29.4	24.3	36.6	25.5	2.3	24.0
0.25–0.5 mm	12.8	32.2	12.9	2.4	12.3	36.4	32.0	33.5	2.5	38.2
<0.25 mm	3.0	32.3	3.1	2.3	2.8	36.2	32.1	33.4	2.4	37.1
Reconstituted	100.0	31.9	100.0	2.5	100.0	100.0	34.8	100.0	2.4	100.0
			Non-Magnetic Fraction								
		Before Attrition **						After Attrition			
	wt.%	%	%Fe %Distrib.	%	%Cr %Distrib.	wt.%	%	%Fe %Distrib.	%	%Cr %Distrib.
1–2 mm	63.1	31.1	63.0	2.6	62.4	0.0				
0.5–1 mm	26.0	31.1	26.0	2.7	26.3	0.8	30.6	0.8	2.6	0.8
0.25–0.5 mm	9.1	31.0	9.1	2.7	9.4	40.7	30.9	40.5	2.6	41.1
<0.25 mm	1.8	31.2	1.8	2.6	1.8	58.4	31.1	58.6	2.5	58.0
Reconstituted	100.0	31.1	100.0	2.6	100.0	100.0	31.0	100.0	2.6	100.0

* The magnetic fraction before attrition is made with all the magnetic fractions recovered from the treatment of the size fractions +0.25–1 mm and +1–2 mm. ** The non-magnetic fraction before attrition is made with all the non-magnetic fractions recovered from the treatment of the size fractions +0.25–1 mm and +1–2 mm.

Table 5. Mass balance of the attrition step performed with several attrition durations on the magnetic fraction.

	wt.%			%Fe			%Cr			%Distrib. Fe			%Distrib. Cr		
Attrition duration (min)	20	40	60	20	40	60	20	40	60	20	40	60	20	40	60
1–2 mm	8.6	3.1	2.4	62.1	85.9	91.7	1.7	0.6	0.3	15.2	7.6	6.1	6.2	0.8	0.3
0.5–1 mm	42.2	24.3	10.3	33.0	36.6	44.5	2.4	2.3	2.3	39.7	25.5	13.2	43.3	23.7	10.0
0.25–0.5 mm	27.3	36.4	31.6	32.1	32.0	32.1	2.4	2.5	2.5	25.0	33.4	29.3	28.0	38.6	33.3
<0.25 mm	21.9	36.2	55.7	32.3	32.1	32.0	2.4	2.4	2.4	20.2	33.4	51.4	22.5	36.9	56.4
Reconstituted	100	100	100	35.1	34.8	34.7	2.3	2.4	2.4	100	100	100	100	100	100

The detailed composition of the size fraction +1–2 mm shows a strong increase in the metallic iron with the attrition duration, the content going from 44.2% after 20 min of attrition to 87.2% after 60 min of attrition (Table 6), while the content of iron oxides decreases (from 24.2% to 6.0%, respectively) as well as the silicate and the spinel phases. Furthermore, the non-milleable fraction, >90 µm, is also increasing. This non-milleable fraction is assumed to be metallic, because of the ductility of metal which forms plates during milling and cannot be further milled and sieved <90 µm. The increase in the metallic iron is associated with a decrease in the mass content of the related fraction (i.e., +1–2 mm),

with values going from 8.6% after 20 min of attrition to 2.4% after 60 min of attrition. Due to the minor amount of this material in a potential feeding mix of a furnace, it could be possible to identify valorization pathways. In particular, the +1–2 mm particles obtained after an attrition of 60 min could be directly used in an EAF while the +1–2 mm particles obtained after an attrition of 20 min could be used for sinter plant/pellet making and blast furnace afterwards.

Table 6. Detailed composition of the size fraction +1–2 mm (Fe-rich particles) obtained after several attrition durations on the magnetic fraction (analyzed according to DIN EN 13656).

In wt.%	20 min Attrition	40 min Attrition	60 min Attrition
>90 µm (Non Milleable Fraction of the Sample, i.e., Not Analyzed)	8	28.6	32.1
Al_2O_3	3.4	1.2	0.5
CaO	9.7	2.8	0.9
Cr(III)	1.7	0.6	0.3
Fe total	62.1	85.9	91.7
Fe metal	44.2	76.8	87.2
FeO	12.2	5.8	3.9
Fe_2O_3	12.0	6.6	2.1
CuO	0.2	0.3	0.3
MgO	1.7	0.5	0.2
MnO	2.8	0.8	0.2
NiO	0.08	0.13	0.16
P_2O_5	0.2	0.06	0.02
S total	0.04	0.01	0.00
SiO_2	4.3	2.1	1.6
TiO_2	0.2	0.06	0.02
V_2O_5	0.09	0.03	<0.02

These results show that magnetic separation led to the separation of some iron-rich/chromium-poor particles even if the chemical analyses of the two fractions obtained after this separation step seemed to indicate that it was not efficient for it. Several characterization methods were then implemented in order to get some understanding of the mechanisms involved in the magnetic separation.

3.2. Characterization of the Magnetic Properties of Each Fraction (Mössbauer Spectroscopy)

Figure 1 shows the Mössbauer spectra of the two fractions obtained after the dry low intensity magnetic separation performed on the size fraction +0.25–1 mm. The spectrum of the magnetic fraction is composed of a magnetic portion and a paramagnetic portion. The magnetic portion is mainly made with metallic iron (α-Fe), with the Fe^{3+} in tetrahedron sites and with the Fe^{2+}/Fe^{3+} in octahedron sites in magnetite (Fe_2O_3). The paramagnetic portion is composed of one singulet and one doublet associated with the Fe^{2+} in wüstite (FeO). Regarding the non-magnetic fraction, the spectrum is only composed of paramagnetic phases with two doublets and one singulet associated with the Fe^{2+} in wüstite (FeO). The quantification of the distribution of iron phases shows that that the main Fe-bearing phase in the magnetic and non-magnetic fractions is a paramagnetic wüstite (Figure 2). However, this paramagnetic wüstite counts for 99% of the iron in the non-magnetic fraction while it counts for 59% in the magnetic fraction with also 44% of the iron in magnetic phases (metallic Fe, magnetite and Fe oxide). Even if all the magnetic phases are found in the magnetic fraction, the presence of paramagnetic wüstite confirms previous results showing that the low intensity magnetic separation was not efficient for the production of a Fe-rich fraction.
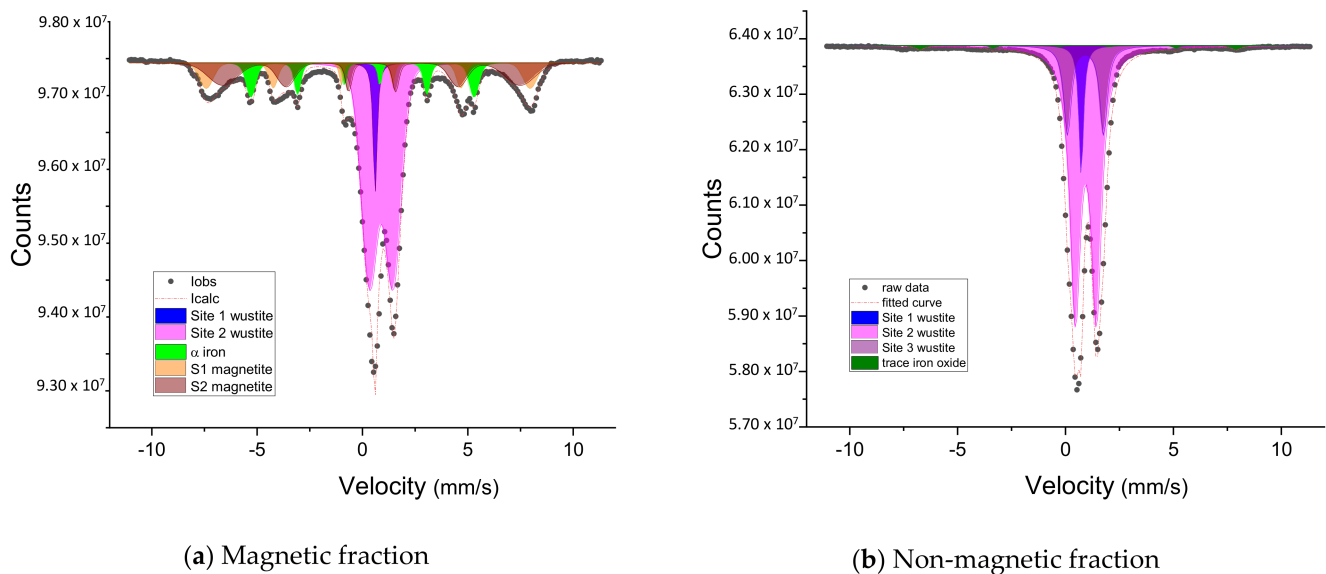
(**a**) Magnetic fraction　　　　　　　　　　　　　　　(**b**) Non-magnetic fraction

Figure 1. Mössbauer spectra of the magnetic (**a**) and non-magnetic (**b**) fractions.
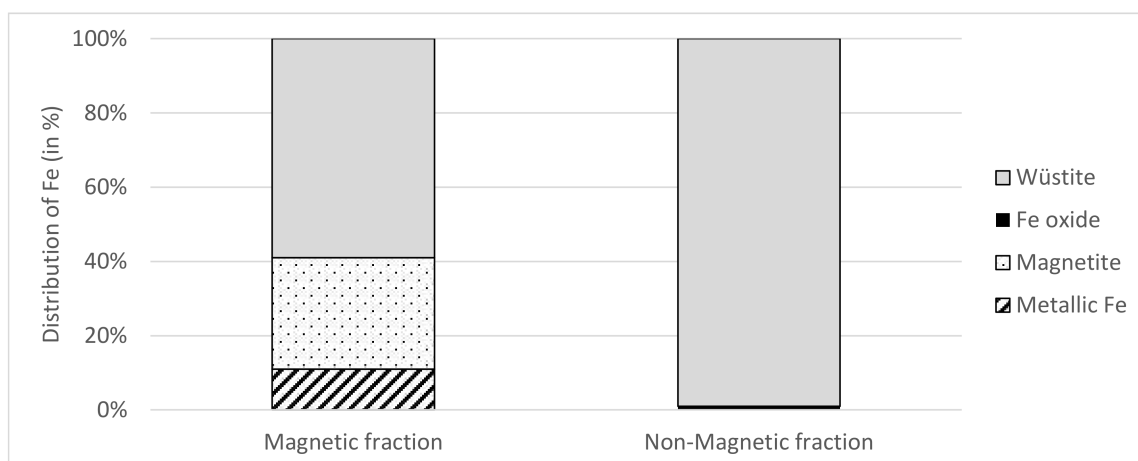

Figure 2. Mössbauer results on iron phases distribution in the samples obtained after dry low intensity magnetic separation of the size fraction +0.25–1 mm.

3.3. Characterization of the Mineralogy and Microstructure

3.3.1. After the Low-Intensity Magnetic Separation

The mineralogy and microstructure of the magnetic and non-magnetic fractions obtained after the magnetic separations performed on the fractions +0.25–1 mm and +1–2 mm were studied. However, only results related to the fraction +0.25–1 mm are presented hereinafter since they show similar trends as to the ones related to the fraction +1–2 mm. Results related to the mineralogy of the fraction +1–2 mm are provided in the Supplementary Material.

The XRD diffractograms of the magnetic and non-magnetic fractions of the sample sized +0.25–1 mm are almost similar at first glance (Figure 3). Mineralogy of the both fractions consist of iron-bearing phases (wüstite, magnetite, maghemite and hematite, magnesiochromite) and silicate phases (larnite, gehlenite and quartz) (Figures 3 and 4). However, Rietveld quantification shows that the magnetic fraction concentrates the magnetite, while the non-magnetic fraction concentrates most of the hematite and a higher share of wüstite. The content of larnite, gehlenite, maghemite, quartz and magnesiochromite/magnesioferrite (these two mineral phases have similar XRD response, it is then difficult to dissociate them) is quite evenly distributed within the two fractions.
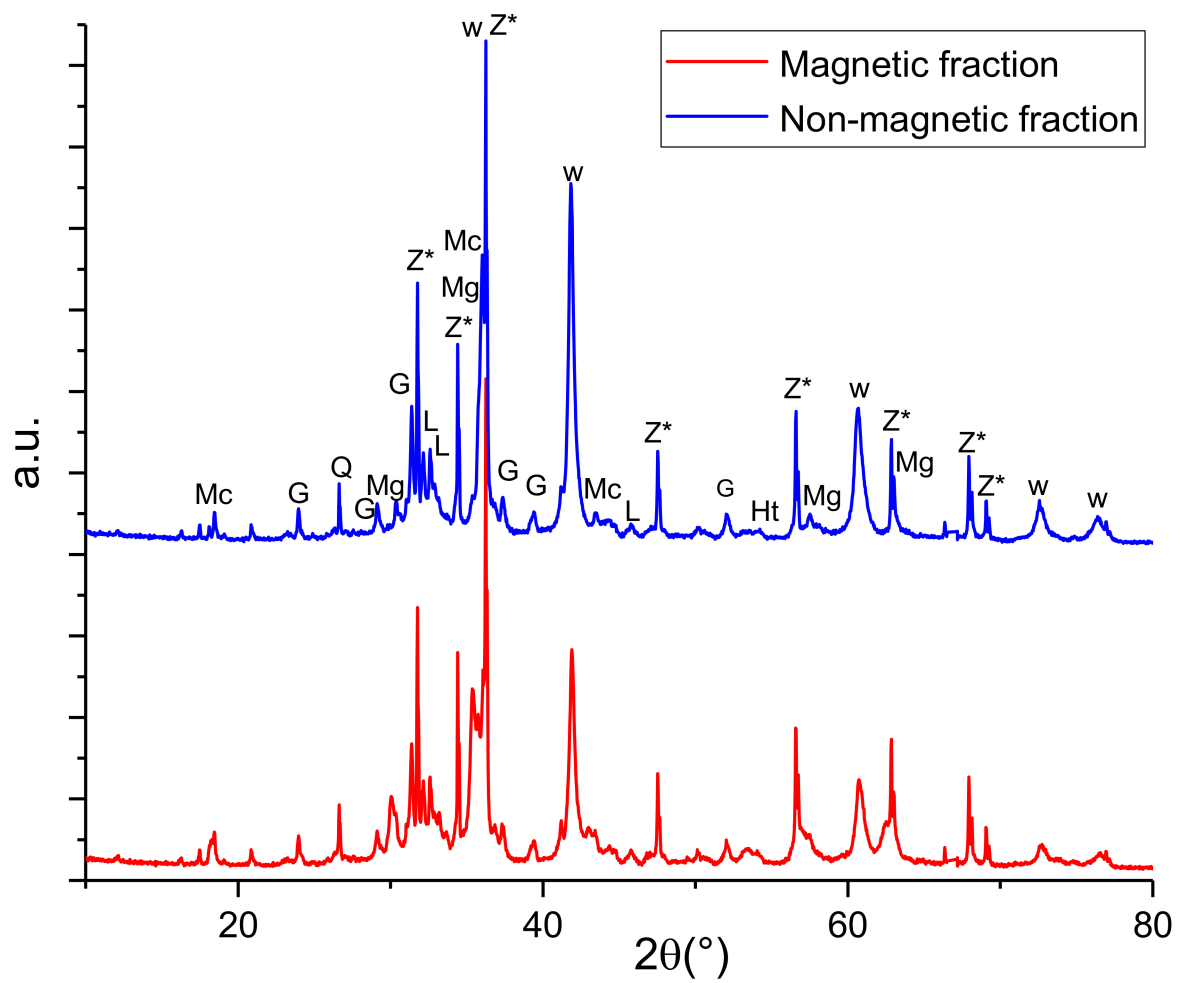
Figure 3. Mineral phases contained in the magnetic and non-magnetic fractions of the size fraction +0.25–1 mm [Mc: Magnesio-chromite, G: Gehlenite, Q: Quartz, Mg: Magnetite, L: Larnite, W: Wüstite, Ht: Hematite and Z*: added zinc oxide] (arbitrary unit for the ordinates).
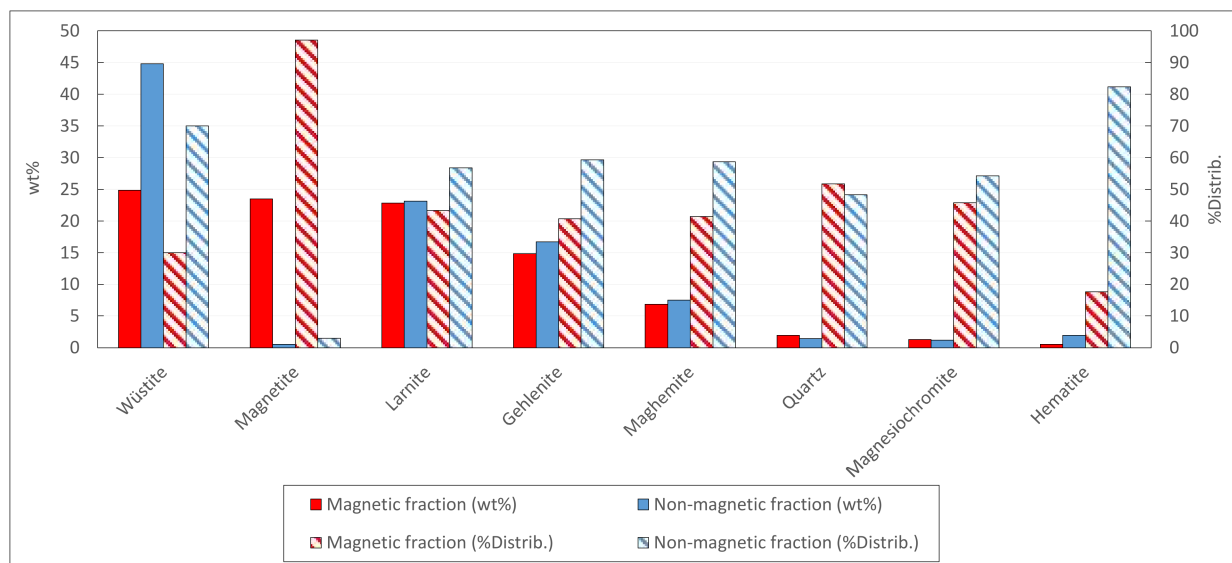

Figure 4. Mineral phases content and distribution in magnetic and non-magnetic fractions of the size fraction +0.25–1 mm.

Microscopic optical observations in reflected light, SEM observations and elemental mapping in SEM allowed determining the nature of the particles and the phase distribution in the two fractions obtained after the magnetic separation of the size fraction +0.25–1 mm.

The magnetic fraction consists of particles with a size +0.5–1 mm which are generally elongated and bright and mixed grains with a size between 50 μm and 1 mm (Figure 5a). Bright particles are made of iron metal. Combined observations at high magnification (view field 300 μm) and elemental mapping shows that mixed grains are aggregates of iron-bearing phases (magnetite) intimately associated with magnesiochromite in a silicate matrix (larnite, gehlenite) (Figure 6). The mineral size in mixed grains varies with the mineral type. The iron-bearing phases have a size of up to 50 μm, usually higher than that of the other phases.
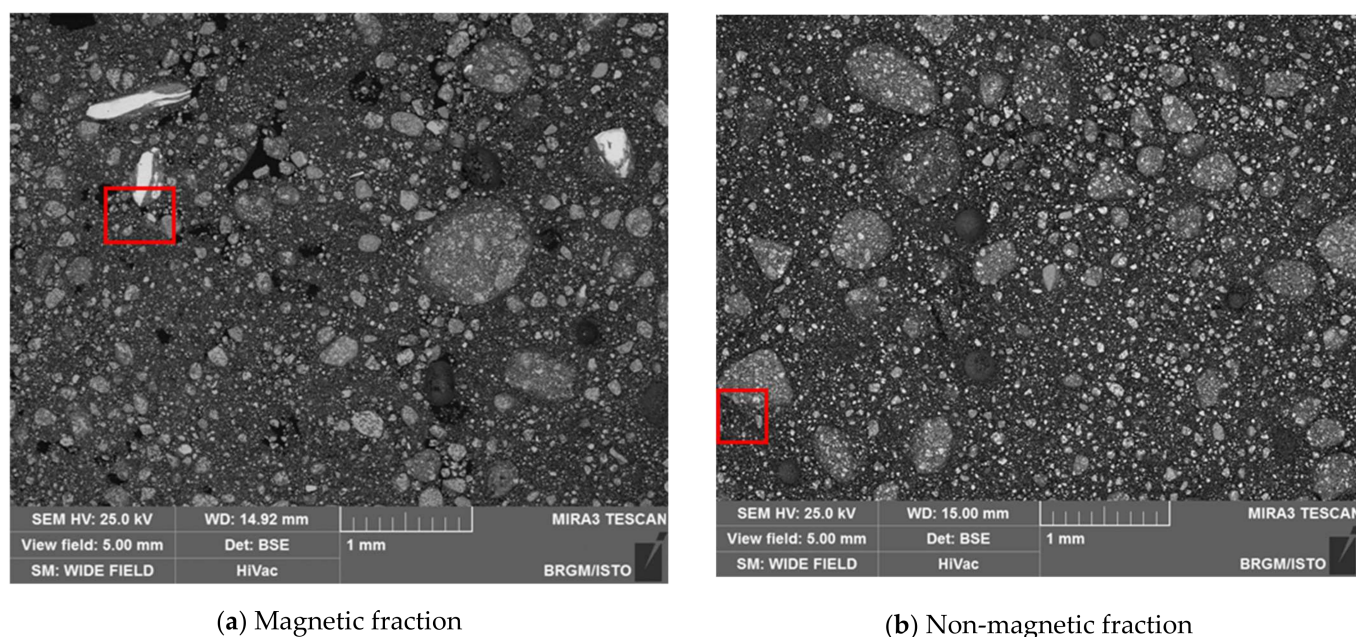

(**a**) Magnetic fraction　　　　　　　　　　　(**b**) Non-magnetic fraction

Figure 5. Textural aspect of the magnetic (**a**) and non-magnetic (**b**) fractions of the +0.25–1 mm-sized fraction and locations of the elemental mapping (red square).

The general aspect of the non-magnetic fraction is very similar to the one of the magnetic fractions, the main difference being the absence of iron metal particles.

Elemental mapping of 8 elements (Fe, Si, Mg, Mn, Al, Cr, Ca and O) in the 0.25–1 mm sized magnetic and non-magnetic fractions are given in Figures 7 and 8, respectively. It can be seen that both fractions contain iron rich particles, as already observed with the XRD analysis. Most of these Fe-rich particles are oxygenated (1). Some of these particles contain manganese and are wüstite-type particles. Others contain manganese, but also aluminum and chromium, and are spinel type particles (magnetite type). Some Fe-rich particles in the magnetic fraction are poorly oxygenated (2–3) and consist of iron metal; such particles are not found in the non-magnetic fraction. Regarding the distribution of chromium, Cr-rich particles can be identified in both fractions, these particles also contain manganese and are spinel type particles. Figures 7 and 8 show that aluminum is associated with calcium and to a lower degree with silicium while magnesium seems to be linked to manganese.

Electron microprobe analyses on both magnetic and non-magnetic fractions of the 0.25–1 mm-sized fraction confirms that the main phases of the slags are iron oxides, including spinel phases, and Ca-silicates as shown by the XRD characterizations. They give further information about mineral composition (Tables 7 and 8). The different iron oxides (wüstite) and Fe-based spinel phases (magnetite-like) were identified on the basis of their iron content, the electron microprobe does not allow separate analysis of Fe^{2+} and Fe^{3+}. Wüstite [FeO] is generally characterized by iron content of 77–78 wt.% Fe and by oxygen

content of ~22–23 wt.% O. Two other types of iron oxides are treated as magnetite-like minerals. Their structural formulas are calculated on the basis of a spinel structure with four oxygens as follows: $(R^{2+})(R^{3+})_2 O_4$, where R^{2+} is filled by divalent cations: Fe, Mn, Mg, and R^{3+} is filled by trivalent cations: Fe, Al, Cr (Tables 7 and 8 and Supplementary data file).
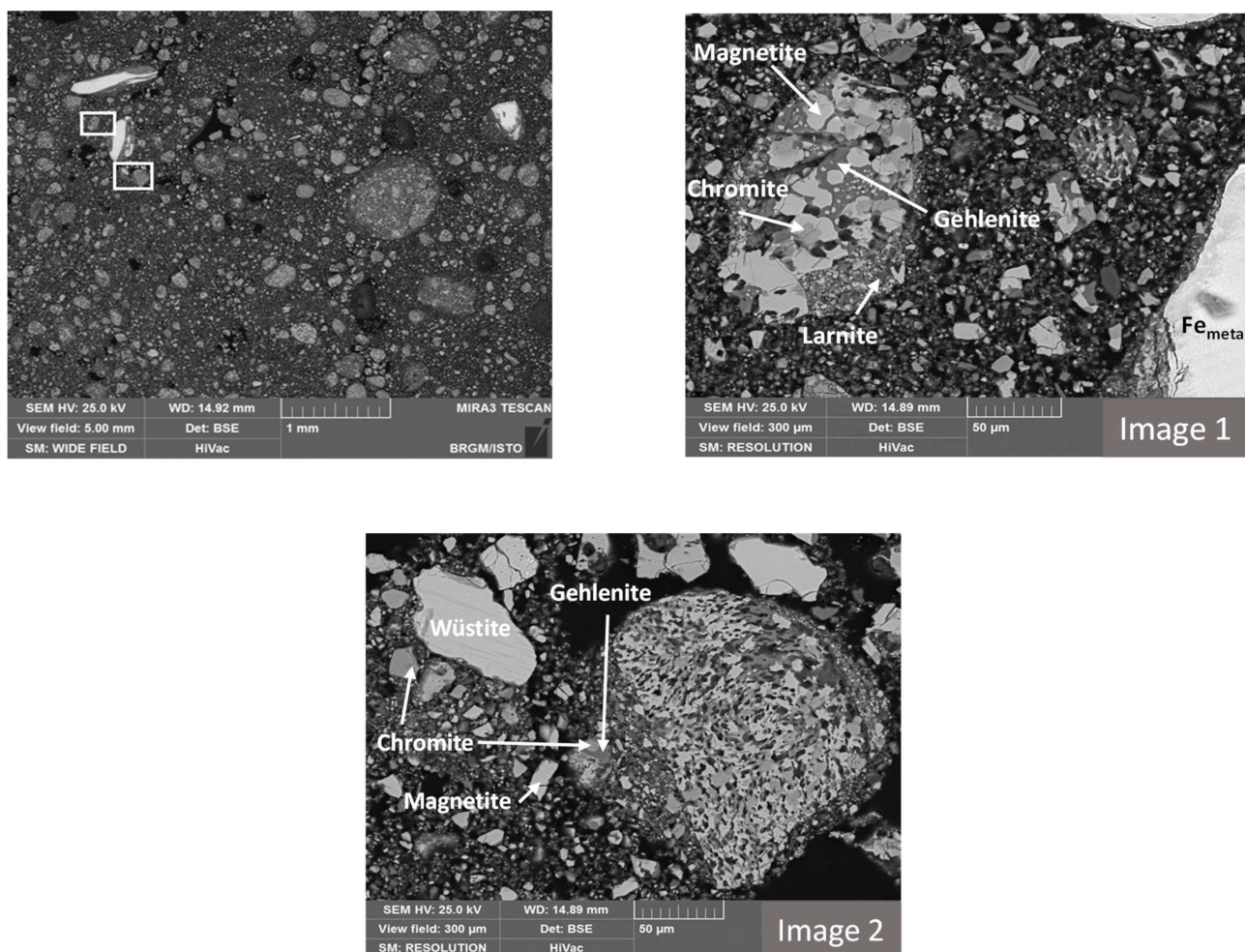

Figure 6. Textural aspect of the magnetic fraction of the +0.25–1 mm-sized fraction with the location of two detailed mineralogical images (white squares).

In the magnetic fraction, analyses of wüstite are iron oxides containing 77.81 ± 2.32 wt.% FeO with a significant substitution of Fe^{2+} by Mn^{2+} (10.93 wt.% MnO) and Mg^{2+} (6.82 wt.% MgO). On the other hand, several compositions of Fe-bearing spinel phases were identified; they are characterized by variable iron content in which a large part of the Fe^{2+} is replaced by Mg and Mn, and a very small part of Fe^{3+} is replaced by Al and Cr. The first composition is characterized by the highest iron content of 70.05 ± 3.62 wt.% equivalent FeO with the following mean structural formula $(Mg_{0.37} Mn_{0.29} Fe_{0.27})(Fe_{1.8} Al_{0.16} Cr_{0.02}) O_4$, composition that corresponds to a magnesioferrite-jacobsite solid solution (called "Fe-rich spinel 1"). The second composition is characterized by lower iron content of 54.83 ± 2.39 wt.% equivalent FeO, and corresponds to the following mean structural formula $(Fe_{0.59} Mg_{0.11} Mn_{0.40})(Fe_{0.95} Al_{0.68} Cr_{0.21}) O_4$ (called "Fe-rich spinel 1"). The third composition is characterized by the lowest iron content of 32.02 ± 7.76 wt.% equivalent FeO, and corresponds to the following mean structural formula $(Fe_{0.34} Mg_{0.11} Mn_{0.40})(Fe_{0.51} Al_{0.97} Cr_{0.50}) O_4$ (called "Fe-rich spinel 1"). The two last compositions differ by the increase in the replacement of Fe^{2+} by Mg and Mn, and the increase in the replacement of Fe^{3+} by Al and Cr, suggesting that these two latter Fe-bearing spinel phases are probably less magnetic than the first

type. Another spinel phase was found and is characterized by high chromium content of 48.98 ± 5.83 wt.% Cr_2O_3, and significant contents of iron, magnesium, manganese and aluminum, corresponding to the following mean structural formula $(Fe_{0.4}Mg_{0.4}Mn_{0.2})$ $(Cr_{1.3}Al_{0.5}Fe_{0.2})$ O_4. This spinel is chemically very similar to magnesiochromite. However, it occurs as rounded grains intimately associated with other Fe-bearing spinels, suggesting this spinel solid solution probably results from an oxidation of a primary wüstite solid solution $(Fe, Mn, Mg)O$ which is metastable in this type of material [14,15]. The gangue consists of larnite (Ca_2SiO_4) and minerals of the melilite group including gehlenite $Ca_2(Fe_{0.5}Mg_{0.1}Al_{0.5})$ $(SiAl)O_7$.
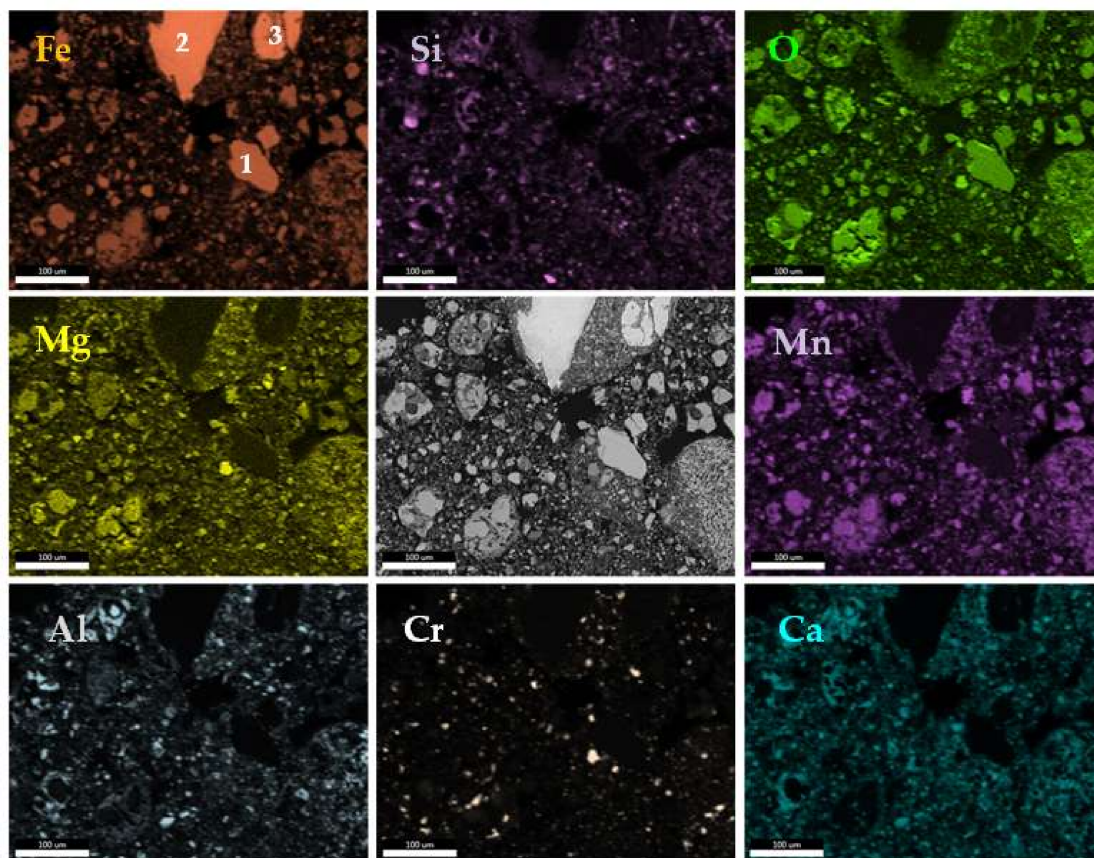

Figure 7. Distribution of some chemical elements in the magnetic fraction of the size fraction +0.25–1 mm determined by EDS 2D mapping in SEM analysis.

In the non-magnetic fraction, the composition of wüstite, Fe-bearing spinel phases and chromite is similar to the one found in the magnetic fraction. However, it is noteworthy that Fe-bearing spinel phases show less variability of chemical composition than in the magnetic fraction. Rare points of the Fe-rich spinel 1 and another Fe-rich spinel (called "Fe-rich spinel 4") have been found in the non-magnetic fraction. These results confirms that the magnetic fraction contains higher Fe-rich mineral phases than the non-magnetic fraction and that chromium is found in Fe-rich spinels and magnesiochromite in both fractions.

3.3.2. After the Attrition

XRD analyzes were performed on the samples produced after an attrition of 40 min of the magnetic and non-magnetic fractions, and in particular on each size fraction obtained after sieving the obtained product (Figures 9 and 10). The XRD diagrams are given in the Supplementary material. It should be mentioned here that it was not possible to analyze by XRD the size fraction +1–2 mm obtained after attrition of the magnetic separation since all this material was previously used for analyzing the detailed chemical composition;

distribution of minerals was then calculated in the various size fractions of the product +0–1 mm after attrition.
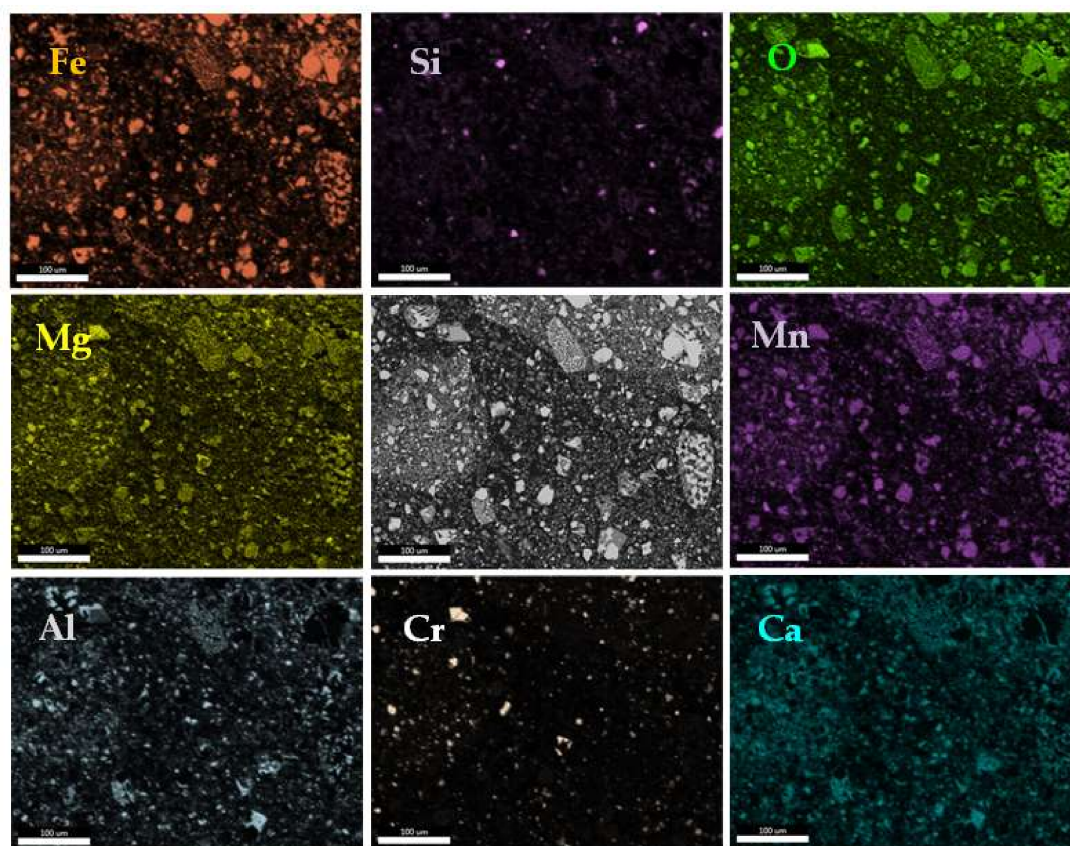

Figure 8. Distribution of some chemical elements in the non-magnetic fraction of the size fraction +0.25–1 mm determined by EDS 2D mapping in SEM analysis.
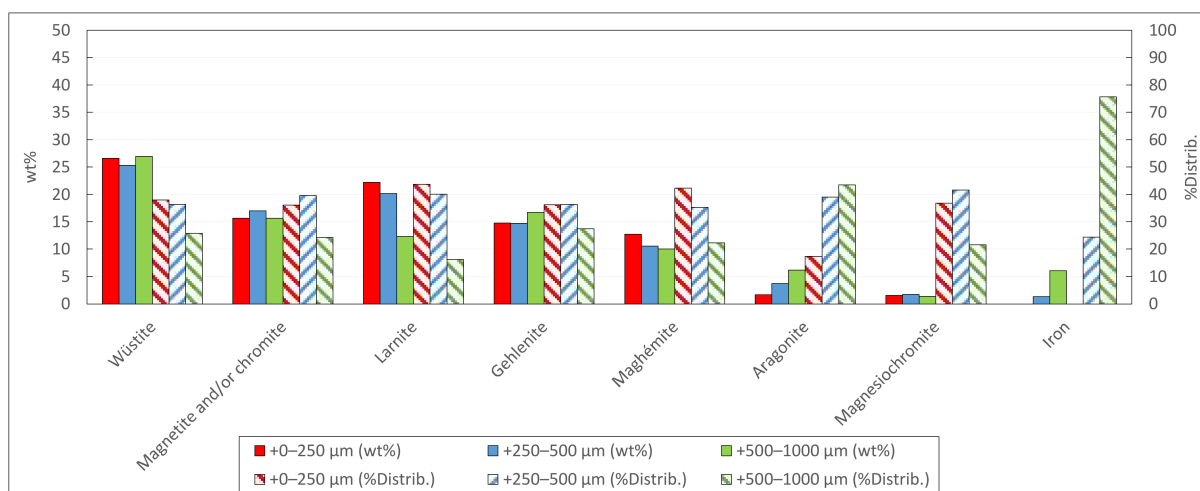

Figure 9. Mineral phases content and distribution in the size fractions +0–250 μm, +250–500 μm and +500–1000 μm after attrition of the magnetic fraction during 40 min.
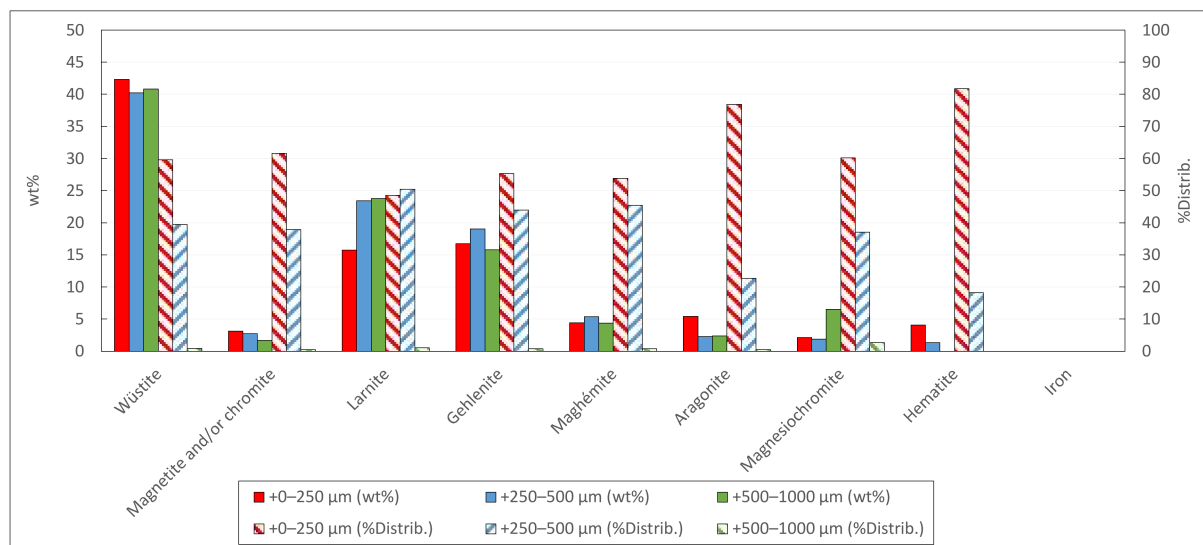
Figure 10. Mineral phases content and distribution in the size fractions +0–250 μm, +250–500 μm and +500–1000 μm after attrition of the non-magnetic fraction during 40 min.

Table 7. Average chemical compositions and standard deviation (σ) of minerals identified in the magnetic fraction. Compositions were acquired using electron microprobe and expressed in weight percent of oxides. The structural formulae were calculated on the basis of the number of oxygen atoms in the mineral (1 for wüstite, 4 for minerals of the spinel group including magnetite and chromite, and 7 for gehlenite), and expressed in atom per formula unit (apfu).

	Metal *	Wüstite		Fe-Rich Spinel 1		Fe-Rich Spinel 2		Fe-Rich Spinel 3		Magnesiochromite		Gehlenite	
		Average	σ	Average	σ	Average	σ	Average	σ	Average	σ	Average	σ
Al$_2$O$_3$	0.03	0.41	0.24	3.92	1.84	17.13	0.67	27.19	10.60	15.06	4.11	34.52	2.42
CaO	0.01	1.44	0.45	2.61	1.34	3.06	4.19	0.86	0.15	1.13	0.91	37.99	2.83
Cr$_2$O$_3$	0.05	0.96	0.55	0.93	0.67	7.92	5.20	20.45	6.55	48.98	5.33	0.14	0.15
FeO	125.14	77.81	2.32	70.05	3.62	54.83	2.39	32.02	7.76	19.97	4.63	5.69	3.22
MgO	0.02	6.82	2.20	7.37	3.18	5.07	0.84	9.70	2.04	10.73	2.32	0.46	0.29
MnO	0.00	10.93	2.75	9.75	3.01	7.89	0.87	6.84	1.49	7.23	2.38	0.56	0.44
P$_2$O$_5$	0.01	0.01	0.02	0.01	0.01	0.00	0.01	0.01	0.01	0.01	0.01	0.09	0.10
SiO$_2$	0.01	0.10	0.12	0.36	0.48	0.05	0.01	0.27	0.32	0.16	0.22	20.87	0.65
V$_2$O$_3$	0.00	0.04	0.02	0.10	0.07	0.26	0.28	0.25	0.06	0.26	0.04	0.06	0.06
Total	125.47	98.57	3.27	95.23	3.72	96.27	1.47	97.43	6.55	103.59	3.20	100.39	2.66
Fe2/Fet		1.00	0.00	0.11	0.06	0.38	0.03	0.44	0.16	0.54	0.15		
nb oxygen atoms		1		4		4		4		4		7	
Al		0.01	0.00	0.16	0.08	0.68	0.02	0.97	0.32	0.54	0.13	1.87	0.09
Cr		0.01	0.00	0.02	0.02	0.21	0.14	0.50	0.16	1.20	0.17	0.01	0.01
V		0.00	0.00	0.00	0.00	0.01	0.01	0.01	0.00	0.01	0.00	0.00	0.00
Fe		0.74	0.06	2.04	0.13	1.55	0.10	0.85	0.28	0.52	0.12	0.22	0.12
Fe3		0.00	0.00	1.80	0.08	0.95	0.08	0.51	0.32	0.23	0.07	0.22	0.12
Fe2		0.74	0.06	0.23	0.15	0.59	0.06	0.34	0.10	0.29	0.12	0.00	0.00
Mg		0.11	0.04	0.37	0.15	0.11	0.02	0.45	0.08	0.49	0.09	0.03	0.02
Mn		0.10	0.02	0.29	0.09	0.40	0.04	0.18	0.06	0.19	0.06	0.02	0.02
Ca		0.02	0.01	0.08	0.06	0.11	0.16	0.02	0.01	0.04	0.03	1.87	0.13
Si		0.00	0.00	0.01	0.02			0.01	0.01	0.01	0.01	0.96	0.02
R2		0.96	0.01	0.89	0.08	1.10	0.02	0.97	0.01	0.97	0.03	0.05	0.04
R3		0.01	0.01	1.99	0.02	1.85	0.11	1.99	0.01	1.98	0.01	2.10	0.09

* Only one point has been found so it is not possible to give an average value and a standard deviation.

Table 8. Average chemical compositions and standard deviation (σ) of minerals identified in the non-magnetic fraction. Compositions were acquired using electron microprobe and expressed in weight percent of oxides. The structural formulae were calculated on the basis of the number of oxygen atoms in the mineral (1 for wüstite, 4 for minerals of the spinel group including magnetite and chromite, and 7 for gehlenite), and expressed in atom per formula unit (apfu).

| | Wüstite | | Fe-Rich Spinel 1 * | Magnesiochromite | | Fe-Rich Spinel 4 | | Gehlenite | |
	Average	σ		Average	σ	Average	σ	Average	σ
Al_2O_3	0.27	0.07	3.18	14.12	3.38	23.40	4.11	35.62	1.94
CaO	1.47	0.42		0.88	0.40	0.85	0.20	39.25	3.05
Cr_2O_3	1.35	0.35	1.93	48.51	3.17	35.41	3.82	0.26	0.63
FeO	78.70	3.53	76.77	23.32	3.61	28.51	4.94	3.69	1.62
MgO	6.83	1.53	6.30	8.23	1.96	8.52	1.92	0.40	0.52
MnO	11.33	2.16	11.00	5.88	0.31	6.16	0.47	0.40	0.31
P_2O_5	0.02	0.01	0.00	0.02	0.04	0.02	0.02	0.05	0.11
SiO_2	0.06	0.07	0.18	0.24	0.45	0.31	0.34	20.69	1.70
V_2O_3	0.09	0.04	0.07	0.30	0.06	0.35	0.04	0.04	0.04
Total	100.14	0.48	99.51	101.58	2.68	103.58	4.30	100.42	3.55
Fe2/Fet	1.00	0.00	0.17	0.68	0.08	0.60	0.04		
nb oxygen atoms	1		4	4		4		7	
Al	0.00	0.00	0.13	0.53	0.11	0.83	0.12	1.93	0.09
Cr	0.01	0.00	0.05	1.23	0.09	0.85	0.08	0.01	0.02
V	0.00	0.00	0.00	0.01	0.00	0.01	0.00	0.00	0.00
Fe	0.74	0.04	2.18	0.63	0.11	0.73	0.14	0.14	0.06
Fe3	0.00	0.00	1.81	0.21	0.07	0.29	0.08	0.14	0.06
Fe2	0.74	0.04	0.37	0.42	0.08	0.43	0.07	0.00	0.00
Mg	0.11	0.02	0.32	0.39	0.08	0.38	0.07	0.03	0.04
Mn	0.11	0.02	0.32	0.16	0.01	0.16	0.01	0.02	0.01
Ca	0.02	0.00	0.00	0.03	0.01	0.03	0.01	1.93	0.12
Si	0.00	0.00	0.01	0.01	0.01	0.01	0.01	0.95	0.07
R2	0.97	0.01	1.00	0.97	0.03	0.97	0.02	0.04	0.05
R3	0.02	0.00	1.99	1.98	0.01	1.98	0.01	2.08	0.12

* Only one point has been found so it is not possible to give an average value and a standard deviation.

Results show the presence of metal iron in the products obtained after attrition of the magnetic fraction, this metal iron being not identified after the attrition of the non-magnetic fraction, mainly in the size fraction 500–1000 μm. Moreover, a higher content of Fe-rich spinels was observed in the attrited products from the magnetic fraction compared to the ones from the non-magnetic fraction, which is due to a higher content of Fe-rich spinels in the whole magnetic fraction obtained just after magnetic separation. Regarding wüstite, its content is quite similar whatever the size fraction after attrition (but higher in the products after attrition of the non-magnetic fraction as already observed in Figure 4), confirming the small liberation size of this mineral. A decrease in the larnite with an increase in the size was observed in the products after attrition of the magnetic fraction, the larnite content being 12.3% in the +500–1000 μm fraction, 20.2% in the +250–500 μm fraction and 22.2% in the +0–250 μm fraction. This is most probably due to the removal of the gangue around the Fe-bearing particles during the attrition. An inverse trend was observed for the larnite in the non-magnetic fraction, with values of 23.8%, 23.4% and 15.7% in the size fractions +500–1000 μm, +250–500 μm and +0–250 μm, respectively. These results may be due to the fact that in the non-magnetic fraction, the larnite is more often finely intertwined with other minerals. After attrition of the non-magnetic fraction, it can also be seen a decrease in the magnesiochromite with a decrease in the size (with a content going from 6.5% to 1.9–2.1% to when the size goes from +500–1000 μm to <500 μm) most probably due to the fact that the magnesiochromite has quite a coarse liberation size.

4. Conclusions

This study focuses on a concentration process for a chromium-bearing carbon steel EAF slag based on a low-intensity magnetic separation performed in a dry mode. The objective is to identify the potential of this technique not only for the recovery of iron particles which could then be re-used for steelmaking but also for the production of a Cr-upgraded fraction which could be used as a basis for chromium recovery.

Results show that even if the magnetic separation seems to be not efficient in a first approach for producing a Fe-rich/Cr-poor fraction, some separation mechanisms still occurred. The main bottleneck for reaching a good separation is most probably the very fine liberation size of the iron and chromium bearing minerals. Indeed, it was observed that the magnetic and non-magnetic fractions are mainly made with mixed particles. However, XRD showed that the magnetic fraction concentrates the magnetite, while the non-magnetic fraction concentrates most of the hematite and wüstite. Moreover, it was observed with the electron microprobe analyses that the magnetic fraction contains more diverse Fe-bearing spinel phases compared to the non-magnetic fraction. A spinel phase characterized by a high chromium content (close to 50%) was found in the magnetic fraction, this spinel being chemically very similar to magnesiochromite.

This "hidden" separation was however revealed by adding an attrition step on the two fractions obtained after magnetic separation. Results showed that attrition of the magnetic fraction led to the production of particles +1–2 mm containing 76.8% of metal iron, the mass weight of this fraction being 3.1%, while this size fraction was totally ground after a similar attrition of the non-magnetic fraction. Metal iron and a higher content of Fe-rich spinels was also observed in the products obtained after attrition of the magnetic fraction compared to the ones from the non-magnetic fraction. Regarding chromium, the concentration steps investigated in this study do not allow to produce a Cr-rich fraction, most probably due to the very fine liberation size of the chromium bearing minerals.

Even if valorization pathways were identified for the iron-rich product, this concentration process may not be profitable from an industrial point of view because of the low amount of material that can be valorized in the steelmaking process and of the difficulty to handle this material due to its fineness. The selective recovery of chromium without any concentration step was then studied within the CHROMIC project and a carbonation treatment was proposed to stabilize the remaining chromium in the matrix material for a potential valorization as a construction material.

Author Contributions: Conceptualization, K.B.; methodology, K.B. and N.M.; formal analysis, K.B., A.S., C.L. and N.M.; investigation, K.B., A.S., C.L. and N.M.; resources, A.M. and D.A.; writing—original draft preparation, K.B., A.S., C.L. and N.M. All authors have read and agreed to the published version of the manuscript.

References

1. Euroslag. Statistics. 2018. Available online: https://www.euroslag.com/products/statistics/statistics-2018/ (accessed on 21 December 2021).
2. Netinger, I.; Bjegovic, D.; Vrhovac, G. Utilisation of steel slag as an aggregate in concrete. *Mater. Struct.* **2011**, *44*, 1565–1575. [CrossRef]
3. Huygens, D.; Saveyn, G.H.M.; Tonini, D.; Eder, P.; Delegado Sancho, L. Technical proposal for selected new fertilizing materials under the Fertilising Products Regulation. *JRC Sci. Policy Rep.* **2019**. [CrossRef]
4. The Government of Italy. *Ministerial Decree n. 186. Regolamento Recante Modifiche al Decreto Ministeriale 5 Febbraio 1998 "Individuazione dei Rifiuti non Pericolosi Sottoposti alle Procedure Semplificate di Recupero, ai Sensi Degli Articoli 31 e 33 del Decreto Legislativo 5 Febbraio 1997, n. 22" (Regulatory that Modified Ministerial Decree Dated 5 February 1998)*; Official Gazette no. 115; The Government of Italy: Rome, Italy, 2006. (In Italian)
5. Shi, C. Steel slag—Its production, processing, characteristics, and cementitious properties. *J. Mater. Civ. Eng.* **2004**, *16*, 230–236. [CrossRef]
6. Skaf, M.; Manso, J.M.; Aragón, A.; Fuente-Alonso, J.A.; Ortega-López, V. EAF slag in asphalt mixes: A brief review of its possible re-use. *Resour. Conserv. Recycl.* **2017**, *120*, 176–185. [CrossRef]
7. Menad, N.; Kana, N.; Seron, A.; Kanari, N. New EAF Slag Characterization Methodology for Strategic Metal Recovery. *Materials* **2021**, *14*, 1513. [CrossRef] [PubMed]
8. Gelfi, M.; Cornacchia, G.; Roberti, R. Investigations on leaching behavior of EAF steel slags. In Proceedings of the Euroslag, Madrid, Spain, 20–22 October 2010.
9. Loncnar, M.; Mladenovič, A.; Zupančič, M.; Bukovec, P. Comparison of the mineralogy and microstructure of EAF stainless steel slags with reference to the cooling treatment. *J. Min. Metall. Sect. B Metall.* **2017**, *53*, 19–29. [CrossRef]
10. Kotás, J.; Stasicka, Z. Chromium occurrence in the environment and methods of its speciation. *Environ. Pollut.* **2000**, *107*, 263–283. [CrossRef]
11. Shen, H.T.; Forssberg, E. An overview of recovery of metals from slags. *Waste Manag.* **2003**, *23*, 933–949. [CrossRef]
12. Horckmans, L.; Möckel, R.; Nielsen, P.; Kukurugya, F.; Vanhoof, C.; Morillon, A.; Algermissen, D. Multi-Analytical Characterization of Slags to Determine the Chromium Concentration for a Possible Re-Extraction. *Minerals* **2019**, *9*, 646. [CrossRef]
13. Lagarec, K.; Rancourt, D.G. Recoil-Mössbauer Spectral Analysis Software for Windows. Version 1.02. 1998.
14. Hazen, R.M.; Jeanloz, R. Wüstite ($Fe_{1-x}O$): A review of its defect structure and physical properties. *Rev. Geophys.* **1984**, *22*, 37–46. [CrossRef]
15. Herbelin, M.; Bascou, J.; Lavastre, V.; Guillaume, D.; Benbakkar, M.; Peuble, S.; Baron, J.-P. Steel Slag Characterisation-Benefit of Coupling Chemical, Mineralogical and Magnetic Techniques. *Minerals* **2020**, *10*, 705. [CrossRef]